Journal of Applied Physics

RESEARCH ARTICLE | JANUARY 05 2026

Enabling broadband low-frequency sound absorption with a stepped Helmholtz-honeycomb metamaterial

Ziming Song ; Wei Chen ; Shengzhe Jin; Feihu Shan; Kui Liu; Hongwei Zhang ; Sichao Qu

J. Appl. Phys. 139, 015105 (2026)
https://doi.org/10.1063/5.0306216

AIP Publishing

Journal of
Applied Physics

ARTICLE

pubs.aip.org/aip/jap

Enabling broadband low-frequency sound absorption with a stepped Helmholtz-honeycomb metamaterial

Cite as: J. Appl. Phys. **139**, 015105 (2026); doi: 10.1063/5.0306216
Submitted: 9 October 2025 · Accepted: 8 December 2025 ·
Published Online: 5 January 2026

Ziming Song,[1] Wei Chen,[1,a)] Shengzhe Jin,[1] Feihu Shan,[1] Kui Liu,[1] Hongwei Zhang,[1] and Sichao Qu[2]

AFFILIATIONS

[1] Beijing Key Laboratory of Power Beam Additive Manufacturing Technology and Equipment, AVIC Manufacturing Technology Institute, Beijing 100024, China
[2] Department of Mechanical Engineering, The University of Hong Kong, Pokfulam 999077, Hong Kong SAR, China

[a)] **Author to whom correspondence should be addressed:** werner_nju@hotmail.com

ABSTRACT

To address the challenge of achieving efficient low-to-mid frequency noise absorption under strict weight and thickness constraints, this study proposes a novel honeycomb structure incorporating stepped multi-cavity Helmholtz resonators (SHRs). The SHR configuration enhances sound absorption in targeted frequency bands through tailored resonance coupling. By integrating theoretical modeling, numerical simulation, and experimental validation, we systematically investigated the influence of step gradient angle, micropore geometry, pore positioning, and structural coupling on acoustic performance. Parametric optimization yielded a half-absorption bandwidth of 350–650 Hz, with the lower cutoff frequency reduced by 39.6% compared to conventional coupled structures (580 Hz). Notably, increasing the gradient angle to 33.7° within a 15 mm cavity depth lowered the resonance frequency by 14.3%, demonstrating the efficacy of gradient tuning for low-frequency control. The proposed structure maintains minimal thickness while significantly improving low-to-mid frequency absorption, offering a promising approach for noise mitigation in complex operational environments.

I. INTRODUCTION

Low-to-mid frequency noise in transportation and industrial environments poses significant health risks and equipment reliability concerns.[1,2] Conventional sound-absorbing structures, however, remain constrained by their large dimensions and limited acoustic efficiency. Acoustic metamaterials have emerged as a prominent research focus in noise control, owing to their capacity—via structural optimization—to achieve substantially superior sound absorption performance at equivalent thicknesses compared to traditional materials.[3] Additive manufacturing technologies further broaden their application prospects by offering considerable design freedom and customization capabilities.[4,5] Therefore, the pursuit of the upper limits of sound absorption through advanced structural design holds considerable promise.

Studies on the underlying acoustic mechanisms of micropores reveal that the interaction between adjacent pores significantly influences performance, with circular apertures demonstrating superior sound absorption compared to narrow slits. Cavity depth and pore diameter have been identified as the most critical governing parameters.[6–8] Notable developments in micropore-based metamaterials include micro-perforated panels (MPPs) with optimized parameters,[9–11] MPPs integrated with auxiliary acoustic structures,[12–15] and those backed by complex cavity configurations.[16–19] Despite their impressive absorption capabilities, these designs often exhibit strong directionality and limited effectiveness when deployed in practical, complex acoustic environments. Helmholtz resonators (HRs) constitute an alternative effective strategy for low- to mid-frequency noise control. Recent advancements have explored various cavity geometries,[20–22] spatial distributions,[23–27] and embedded apertures,[28–31] achieving effective absorption within the 132–930 Hz range. Nevertheless, a trade-off between performance and compactness persists, as most high-efficiency designs exhibit substantial thicknesses—typically exceeding 40 mm—which severely limits their practical applicability. Honeycomb structures are widely recognized for their high spatial efficiency and exceptional out-of-plane compressive and shear strength, rendering them ideal for thin yet mechanically robust designs. In acoustic metamaterials, honeycomb-based systems demonstrate superior low-frequency sound absorption,[32] especially when coupled with micro-perforated panels (MPPs),[33] with the primary energy dissipation mechanism localized at the aperture necks.[34,35] Further absorption enhancements have been achieved by strategically tailoring the internal configuration of the honeycomb cells.[36–38] Collectively, these advances underscore the significant potential of honeycomb structures, yet they also reveal two persistent challenges: excessive structural thickness and suboptimal spatial efficiency.

Based on this integrated approach, a honeycomb-structured metamaterial composed of multiple coupled Helmholtz resonators is proposed. The design concurrently provides substantial low-to-mid frequency sound absorption and enhanced mechanical strength endowed by its hexagonal honeycomb configuration. These attributes make it particularly suitable for space-constrained, high-noise environments, including high-speed train cabins, aircraft fuselages, and ship compartments.

II. METHOD AND DESIGN

A. Structural design

The proposed stepped multi-cavity Helmholtz resonator (SHR) structure employs a multi-dimensional stepped configuration of trapezoidal Helmholtz resonators to achieve targeted sound absorption. As illustrated in Fig. 1(a), the unit cell features a multi-level composite architecture, with a regular hexagonal honeycomb cavity serving as the outer envelope. Within this cavity, a central hexagonal prism forms the main chamber, surrounded radially by 12 trapezoidal sub-cavities. The depths of these sub-cavities follow a defined gradient angle β_{∇} along the radial direction [Eq. (1)], resulting in a highly asymmetric height distribution. Figures 1(b)–1(c) provide a parametric visualization of the design concept, where light blue areas represent Helmholtz resonator volumes and light purple denotes the outer micro-perforated panel surface. Light purple arrows trace the sound wave propagation path through the structure. Key geometric parameters include upper aperture diameter (D), intermediate aperture diameter (d), distance between the top micropore and sidewall (w), vertical distance from the ith intermediate micropore to the top surface (y_i), wall thickness (t), and total cavity depth (H),

$$\beta_{\nabla} = \tan^{-1}\left(\frac{h_6 - h_1}{k_{\nabla}}\right). \tag{1}$$

In Eq. (1), the gradient coefficient k_{∇} is determined by the base length of the unfolded unit cell; a value of k_{∇} = 16.5 is adopted in this design. Given that the intermediate micropore diameter is d = 1.5 mm, the resulting cavity segment height h_i must not be less than 1.5 mm. The degree of structural gradient increases with β_{∇}.

By strategically positioning micropores away from the central axis, the SHR structure directs sound waves to pass through multiple layers of micro-perforated panels before entering the Helmholtz resonators, thereby enhancing energy dissipation. In contrast to conventional absorbers limited to one-dimensional resonator arrangements, the SHR design enables multidimensional resonator layouts. This significantly increases the number of resonators integrated into a single structural unit, improving low-frequency sound absorption performance within a confined spatial envelope.

B. Theory analysis

Compared with conventional honeycomb units, the SHR exhibits a more intricate cavity configuration within each periodic element. Based on the structural layout depicted in Fig. 1(c) and under the assumption of acoustically rigid honeycomb cell walls, the sound absorption coefficient of each cavity can be determined using the acoustic impedance formula as follows:[39]

$$\alpha = 1 - |R|^2 = 1 - \left|\frac{Z_s/Z_0 - 1}{Z_s/Z_0 + 1}\right|^2, \tag{2}$$

where R represents the reflection coefficient, Z_s is the surface impedance of the unit, and Z_0 is the characteristic impedance of air, which is the product of air density (ρ_0) and sound speed (c_0).

The overall acoustic impedance Z_s of this composite sound-absorbing structure results from the series and parallel coupling of its constituent components. Here, Z_{pD} denotes the acoustic impedance of the primary surface micropore, and Z_{pd} represents the acoustic impedance of the secondary (intermediate) micropore, evaluated after sound transmission through the first cavity. They can be given by[39,40]

$$Z_{pD} = \frac{32\eta t_1}{\sigma_1 D_1^2}\sqrt{1 + \frac{r-1}{\sqrt{Pr}}} + \frac{j\omega(t_1 + 0.85D)}{\rho_0 c_0}, \tag{3}$$

$$Z_{pd} = \frac{32\eta t_2}{\sigma_2 d_1^2}\sqrt{1 + \frac{r-1}{\sqrt{Pr}}} + \frac{j\omega(t_2 + 0.85d)}{\rho_0 c_0}, \tag{4}$$

where η is the dynamic viscosity of air, ρ_0 is the air density, c_0 is the speed of sound, t_1 and t_2 are the thicknesses of the micro-perforated plates, D and d are the diameters of the top and middle micropores, γ is the specific heat ratio, Pr is the Prandtl number, and $\omega = 2\pi f$ is the angular frequency of the incident sound wave.

Upon sound wave transmission through an unsealed cavity, its acoustic impedance is modeled via acoustic compliance. Accordingly, Z_{c1} denotes the acoustic compliance between Z_1 and Z_2, while Z_{c2} represents that of the intermediate slender cavity, given by the expressions,[41]

$$Z_{ci} = -j\frac{\rho_0 {c_0}^2}{\omega V_i}, \tag{5}$$

where V_i is the volume of the corresponding cavity.

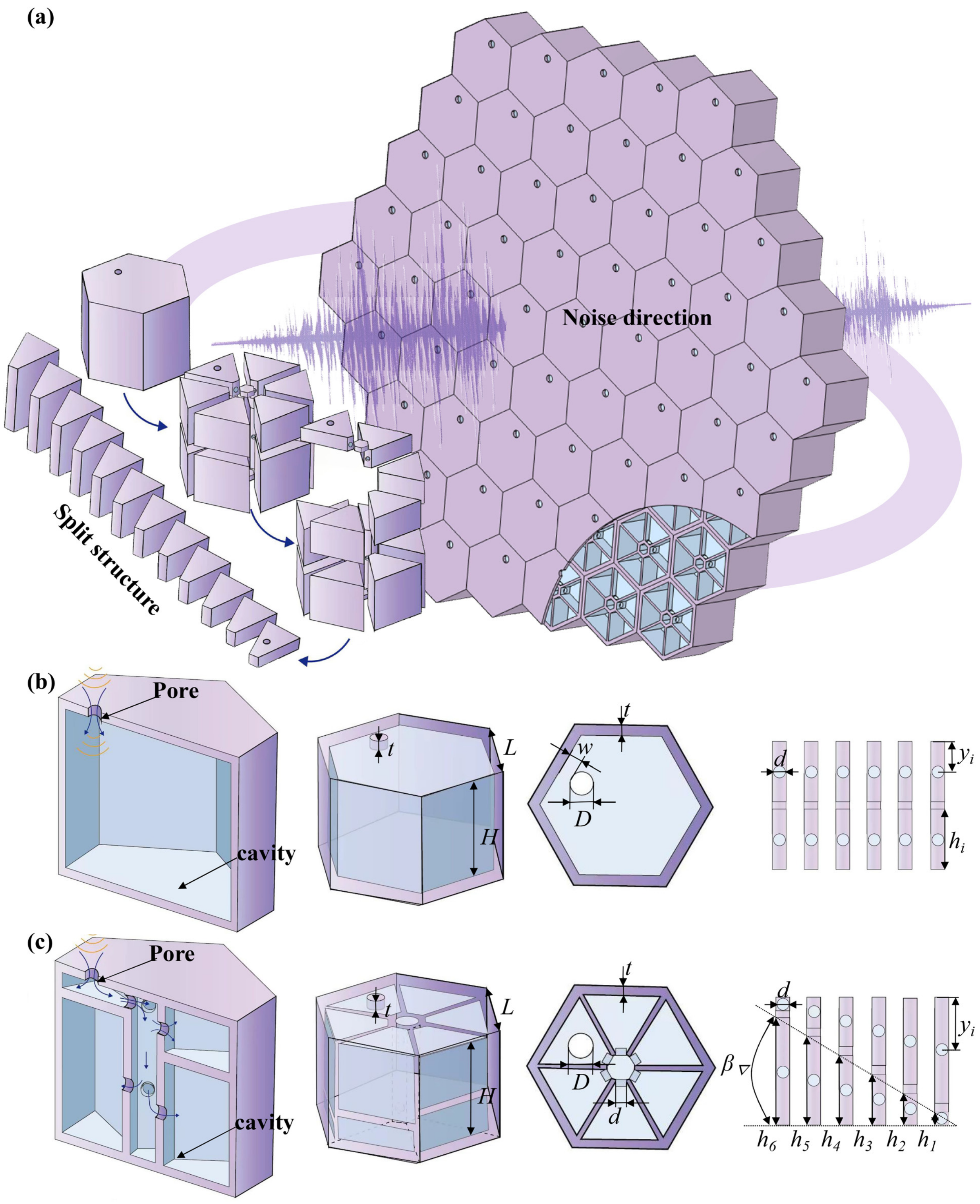

FIG. 1. Structural design of the SHR structure: (a) overall configuration; (b) detailed parameters of the conventional structure; and (c) detailed parameters of the SHR structure.

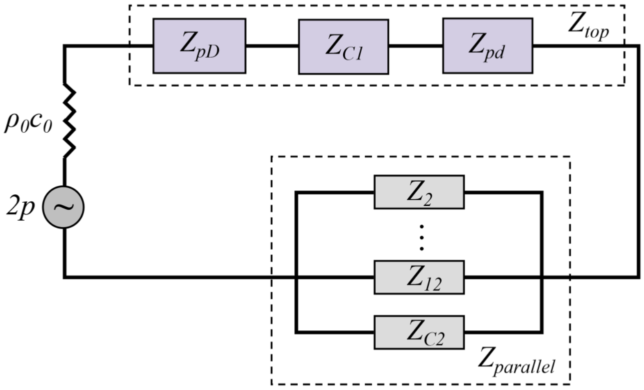

FIG. 2. Equivalent circuit diagram.

The resonance coupling mechanism in the SHR structure arises from the interaction between the primary Helmholtz resonance and the stepped sub-cavities. While sound entering the intermediate slender cavity subsequently propagates into individual Helmholtz resonators, modeling the sound pressure distribution and volume velocity allocation necessitates treating the acoustic compliance Z_{c2} of the slender cavity in parallel with the impedances of the 11 Helmholtz cavities. The resulting equivalent impedance is denoted, $Z_{parallel}$, as[42,43]

$$Z_{parallel} = \left(\frac{1}{Z_{c2}} + \sum_{i=2}^{12} \frac{1}{Z_i}\right)^{-1} = \left(-\frac{\omega V_2}{j\rho_0 {c_0}^2} + \sum_{i=2}^{12} \frac{1}{r(D,t) + j\omega\left[m(D,t) - \frac{\rho_0 {c_0}^2}{\omega V_i}\right]}\right)^{-1}, \quad (6)$$

where Z_i is the acoustic impedance of the ith Helmholtz cavity and the step gradient angle β_∇ directly influences V_i, thereby altering the resonance frequency of each sub-cavity. The coupling between adjacent cavities enhances the phase cancellation and energy dissipation across multiple frequencies, leading to a broader absorption bandwidth. r(D,t) is the acoustic resistance, and m(D,t) is the acoustic mass reactance, which satisfy the following expressions:

$$r(D,\, t) = \frac{32\eta t}{\rho_0 c_0 D^2}\sqrt{1 + \frac{k^2}{32}}, \quad (7)$$

$$m(D,\, t) = \frac{t}{\rho_0 c_0}\left(1 + 0.85\frac{D}{t}\right), \quad (8)$$

$$k = \frac{D}{2}\sqrt{\frac{\omega \rho_0}{4\eta}}. \quad (9)$$

Therefore, $Z_{parallel}$ is expressed as

$$Z_{parallel} = \left(-\frac{\omega V_2}{j\rho_0 {c_0}^2} + \sum_{i=2}^{12} \frac{1}{\frac{32\eta t}{\rho_0 c_0 D^2}\sqrt{1 + \frac{D^2 \omega \rho_0}{512\eta}} + j\omega\left[\frac{t}{\rho_0 c_0}\left(1 + 0.85\frac{D}{t}\right) - \frac{\rho_0 {c_0}^2}{\omega V_i}\right]}\right)^{-1} \quad (10)$$

In summary, upon entering through the surface micropore Z_{pd}, a portion of the incident acoustic energy is shunted by the first cavity Z_{c1}, while the remainder propagates through the intermediate micropore Z_{p2} into a lumped-parameter network comprising the slender cavity and the 11 Helmholtz resonators. The overall acoustic impedance Z_s of the composite structure is derived from the series and parallel combination of these components, as represented by the equivalent circuit in Fig. 2, and is given by the following expression:

$$Z_s = Z_{top} + Z_{parallel}. \quad (11)$$

In this formulation, $Z_{top} = Z_{pd} + Z_{c1} + Z_{pD}$ represents the total impedance of the upper section, while all other variables retain their previously defined meanings. The incorporation of multiple resonators broadens the range of internal oscillations, shifting energy dissipation from being predominantly governed by micropore damping to being substantially enhanced by resonant mechanisms. This modeling approach provides a more rigorous explanation for the variation in acoustic impedance with pore positioning, thereby establishing a consistent mathematical foundation for the underlying acoustic theory.

C. Simulation and experimental studies

A three-dimensional finite element model (FEM) was developed in COMSOL Multiphysics® to investigate the underlying sound absorption mechanisms of the honeycomb SHR structure. The model incorporated the pressure acoustics and thermoviscous acoustics modules.[43–47] As illustrated in Fig. 3(b), the mesh was constructed based on the geometry in Fig. 3(a), with the following dimensions: hexagonal side length L = 10 mm, cavity depth H = 15 mm, wall thickness t = 1 mm, and both top (D) and middle (d) micropore diameters equal to 1.5 mm. The top micropore was located at the centroid of the trapezoidal cavity, and the gradient angle was set to its maximum value. All structural walls were treated as acoustically rigid boundaries. The thermoviscous acoustics module, accounting for boundary layer effects, was used to capture acoustic behavior and energy dissipation in the micropore necks and cavity air domains. A background pressure field was applied to simulate an incident plane wave propagating along the Z-direction, while a perfectly matched layer (PML) served as an anechoic termination at the top boundary. To reflect the structural periodicity, periodic boundary conditions were imposed in all three directions at the top domain of the model. The sound absorption coefficient of the SHR unit was subsequently computed using Eq. (2).

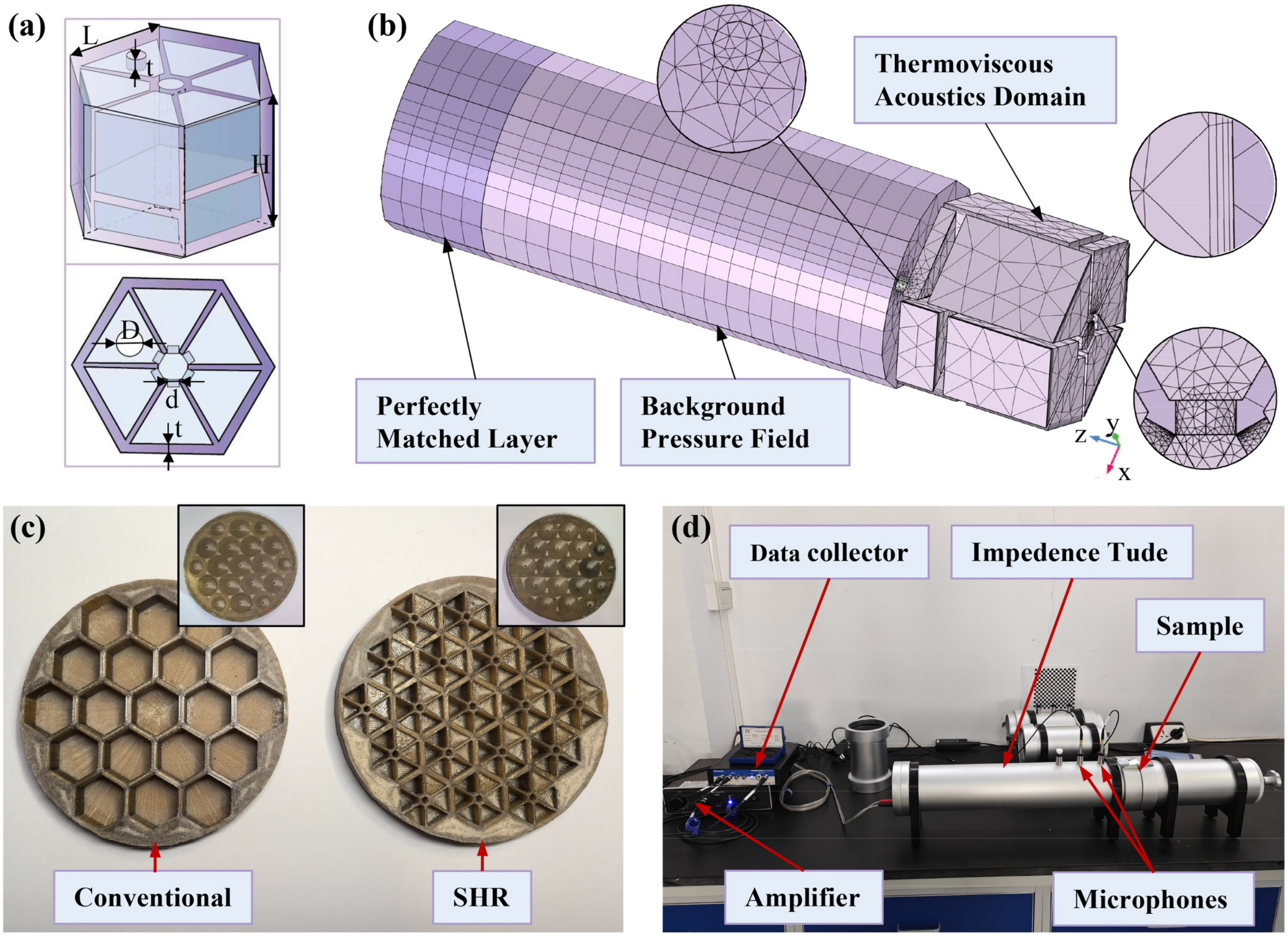

FIG. 3. Experimental setup and specimens: (a) the 3D parametric model of the SHR structure; (b) 3D FEM of the SHR structure; (c) 3D printed structures by FDM; and (d) impedance tube apparatus.

Given the structural miniaturization and high precision requirements, the specimens were fabricated using additive manufacturing. Poly(ether-ether-ketone) (PEEK) was selected as the printing material due to its high modulus, strength, toughness, and impact resistance, along with a density of 1300 kg/m^3, sound speed of 3420 m/s, and a manufacturing tolerance of ±0.2 mm, Sensitivity analysis reveals that variations in micropore diameter within this tolerance range cause resonance frequency shifts of 7–12 Hz. Both the conventional honeycomb and SHR specimens were produced via high-temperature fused deposition modeling (FDM), each with a diameter of 95 mm and a total thickness of 16 mm—comprising a 1 mm-thick micro-perforated panel and a 15 mm deep cavity. To ensure controlled variable comparison between simulation and experiment, the SHR structure maintained the same geometric configuration as depicted in Fig. 3(a), with the top micropores of both structures positioned adjacent to the honeycomb unit sidewalls. The 3D printed structures by FDM are shown in Fig. 3(c).

The sound absorption coefficients across the 200–1200 Hz frequency range were measured using a BSWA SW4201 impedance tube with the two-microphone transfer function method, as depicted in Figs. 3(c) and 3(d). All tests were conducted under controlled ambient conditions to minimize environmental interference. The impedance tube measurements were conducted under controlled environmental conditions (temperature: 23 ± 1 °C, relative humidity: 50 ± 5%). Prior to testing, the microphones were calibrated using a pistonphone calibrator to ensure measurement accuracy within ±0.2 dB. Specimens were sealed against the tube using elastic gaskets to minimize edge effects and ensure rigid boundary conditions. Each specimen was mounted at one end of the tube while acoustic excitation was applied at the opposite end. Two microphones, positioned midway along the tube, captured the

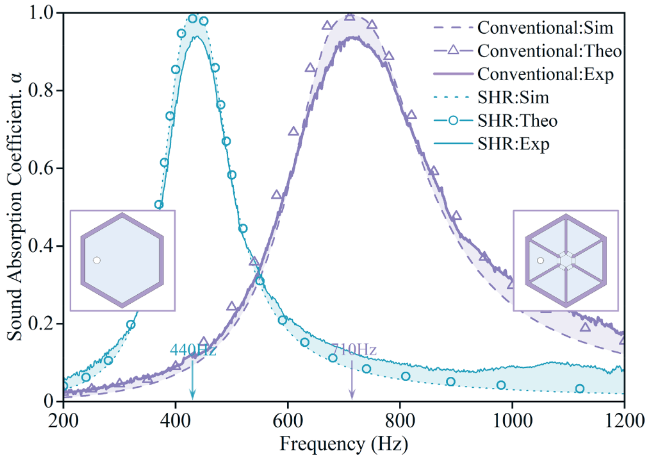

FIG. 4. Sound absorption coefficients of numerical simulation, theoretical calculation, and experimental measurement.

incident and reflected pressure waves, enabling the subsequent calculation of the sound absorption coefficients.

Figure 4 presents the sound absorption coefficient distributions of conventional honeycomb and SHR structures across the 200–1200 Hz frequency range. Thorough verification reveals that the observed discrepancies primarily originate from thin walls induced by manufacturing tolerances, particularly between Helmholtz resonators with similar volumetric shapes. These thin walls create unintended acoustic interference among internal cavities, leading to reduced peak values. The design concept is thereby confirmed: under identical dimensional constraints, the SHR structure exhibits a substantially lower resonance frequency than its conventional counterpart. Specifically, the SHR resonance occurs below 440 Hz, compared to over 710 Hz for the conventional honeycomb—a reduction of approximately 38%. This significant frequency shift underscores the enhanced low-frequency absorption capacity of the SHR design at equivalent cavity depth, highlighting its potential for practical noise control applications.

III. PARAMETRIC STUDIES

A. Structural gradient effect

Following thorough validation of the simulation reliability via theoretical analysis, we next examine the influence of the stepped configuration on acoustic performance. The base model maintained a total cavity depth of $H = 15$ mm, incorporating 12 internally distributed cavities, a hexagonal side length $L = 10$ mm, and a micropore plate thickness $t = 1$ mm. Both the top (D) and middle (d) micropore diameters were set to 1.5 mm, with the top micropore positioned at the centroid of the first cavity. Guided by Eq. (1), the acoustic effects of four gradient angles β_{∇} ranging from 0° to 33.7° were systematically evaluated. The corresponding geometric dimensions are summarized in Table I.

Figure 5(b) illustrates the energy dissipation distribution within a single SHR unit for different gradient angles, with color intensity corresponding to dissipation magnitude. Numerical simulations indicate that maximum dissipation occurs near the micropores due to boundary layer effects, while the remaining energy is attenuated toward the cavity interiors. As the gradient angle increases, energy dissipation near the primary micropores intensifies by 35%, and a more pronounced enhancement of 54% is observed around the originally weaker bottom micropores, attributable to reinforced resonant coupling.

Further analysis reveals that total acoustic dissipation stems from energy losses within both the cavities and interstitial regions. Figures 5(a) and 5(c) compare the sound absorption coefficients across different gradient angles and quantify corresponding shifts in resonance frequency and bandwidth for absorption coefficients above 0.8. The results show a 14.3% reduction in resonance frequency with increasing gradient angle. Moreover, within the constraint of total cavity depth H, the structure with the maximum gradient angle β_{∇} achieves absorption coefficients exceeding 0.8 over the 440–530 Hz range. These findings highlight the crucial role of gradient angle in governing the acoustic behavior of the SHR structure and validate the advantage of parametrically graded designs for low-to-mid frequency absorption.

B. Influence of micropore parameters

Owing to the multi-channel micropore configuration of the structure, acoustic losses are predominantly localized near the micropores, necessitating a systematic investigation into the effect of micropore geometry on sound absorption performance. To maintain structural consistency, the gradient angle β_{∇} was fixed at its maximum value of 33.7° for the unit thickness, while the honeycomb dimensions remained identical to those in the numerical model ($t = 1$ mm, $H = 14$ mm, and $L = 10$ mm). The SHR design features two types of micropores: one set located at the top of the honeycomb unit, and another arranged in a stepped distribution along the sides of the central vertical channel. By selectively varying the diameter and relative position of each micropore set,

TABLE I. Dimensional relationship between cavity depth h and gradient angle β_{∇}.

β_{∇}	h_1	h_2	h_3	h_4	h_5	h_6	h_7	h_8	h_9	h_{10}	h_{11}	h_{12}
0°	7.0	7.0	7.0	7.0	7.0	7.0	7.0	7.0	7.0	7.0	7.0	7.0
16.86°	4.5	5.5	6.5	7.5	8.5	9.5	4.5	5.5	6.5	7.5	8.5	9.5
31.22°	2.0	4.0	6.0	8.0	10.0	12.0	2.0	4.0	6.0	8.0	10.0	12.0
33.70°	1.5	3.7	5.9	8.1	10.3	12.5	1.5	3.7	5.9	8.1	10.3	12.5

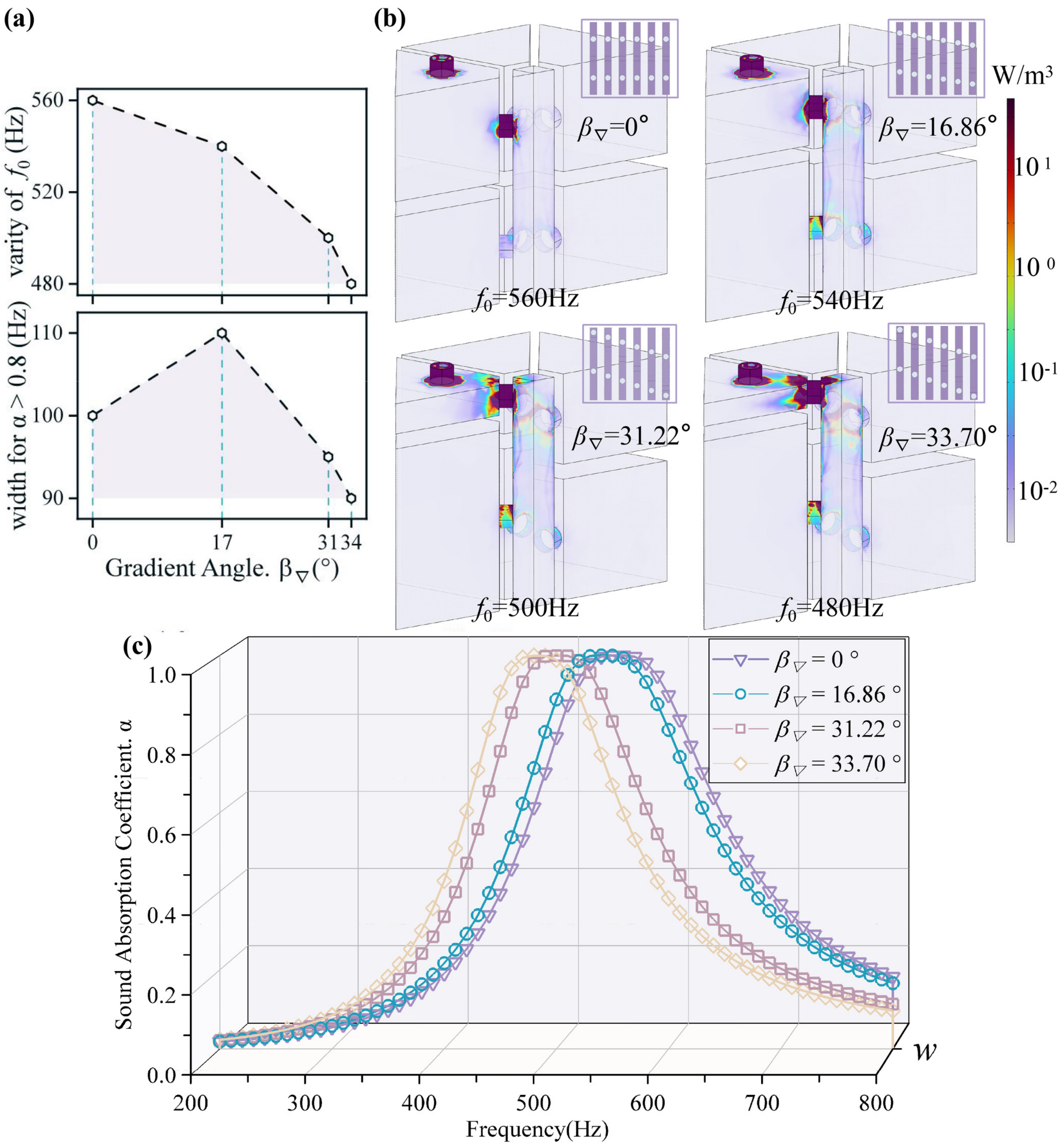

FIG. 5. Acoustic performance of SHR structures with varied gradient angles: (a) resonance frequency shift and broadband absorption ($\alpha > 0.8$); (b) thermoviscous energy dissipation distribution; and (c) comparative absorption spectra.

their individual influence on energy dissipation and overall sound absorption performance was evaluated.

1. Influence of top micropore parameters

The top micropores function as the primary parallel acoustic resistance, coupling the internal cavities with the external environment. Their energy dissipation is governed mainly by thermoviscous losses, which are influenced by boundary layer effects—making the relative position of the micropores a relevant parameter for analysis. This positional relationship is characterized by the distance w between the micropore edge and the inner cavity wall. Using the same honeycomb dimensions as in Sec. III A, SHR units with three top micropore diameters D (1.0, 1.5, and 2.0 mm) and three edge-to-wall distances w (0, 1.2, and 2.4 mm) were systematically analyzed.

Further analysis of the thermoviscous acoustic field elucidates the energy dissipation mechanism associated with the top micropores. As demonstrated in Figs. 6(a) and 6(b), numerical simulations reveal two key trends: as the top micropore diameter decreases, thermoviscous losses become increasingly concentrated around the pore, with their relative proportion rising from 57% to 80%. Owing to the stepped configuration of cavity depths which increase clockwise from beneath the top micropore, a comparison of dissipation across the six regions in the same layer shows that the dissipation in each of the other five cavity scales with its depth difference relative to the cavity directly below the top micropore. A greater depth difference results in stronger energy dissipation. Simultaneously, a reduction in the sidewall distance w enhances the boundary layer effect, intensifying dissipation near the sidewall by approximately 27%.

Figures 6(b)–6(d) illustrate the influence of the two top micropore parameters on the sound absorption coefficient. The results indicate comparable peak absorption coefficients at resonance for both parameters. However, the resonance frequency decreases by 21.4% as the top micropore diameter D is reduced and by 10% as the sidewall distance w decreases. This demonstrates that, among the top micropore parameters, diameter D exhibits the highest sensitivity—a conclusion further supported by the Pareto chart in Fig. 6(d). Thus, optimizing the top micropore parameters offers an effective approach for tuning the low-frequency absorption range of the SHR structure.

2. Influence of middle micropore parameters

The middle micropores serve as the final-stage parallel acoustic resistance, linking the central vertical cavity to individual subcavities, with their diameter designated as d. Adopting the same honeycomb geometry as in Sec. III A and considering the acoustic interference range, the axial separation between the middle and top micropores is identified as a key factor influencing sound absorption performance. Given the varying height h of each cavity, the average axial distance from the middle micropores to the top surface is calculated as follows (unit: mm):

$$y_{average} = \frac{1}{12}\sum_{i=1}^{12} y_i, \tag{12}$$

where y_i denotes the axial distance from the middle micropore of the ith cavity to the top surface. Based on the cooperative Helmholtz resonance mechanism, the acoustic dissipation behavior was analyzed with respect to the diameter and position of the middle micropores. Figure 7(a) shows the energy dissipation distributions at resonance for SHR units with different middle micropore diameters d and average axial distances $y_{average}$. The results indicate that a reduction in d increases the thermoviscous loss around the pore itself by 19%, consistent with the behavior observed at the top micropore. More notably, due to the modified cavity channel volume, the thermoviscous loss at the corresponding middle micropore in the adjacent layer increases by 65%. This substantial enhancement underscores the significant influence of the middle micropore diameter on the global resonance behavior. Furthermore, as $y_{average}$ increases, thermoviscous losses along the sidewalls of the central hexagonal channel rise markedly, leading to a total dissipation increase of approximately 25%.

The sound absorption coefficients obtained from numerical simulations for the two parameters are plotted in Fig. 7(b). Results show that the resonance frequency decreases by 13.0% as the middle micropore diameter d is reduced and by 12.3% as the average axial distance $y_{average}$ increases. The Pareto chart in Fig. 7(d) indicates that both parameters exert a similar influence on the absorption bandwidth of the SHR structure. However, as shown in Fig. 7(c), reducing d lowers the average peak absorption coefficient from 0.982 to 0.910—a 7.3% reduction—while varying $y_{average}$ maintains nearly constant peak absorption. Therefore, to achieve a target resonance frequency, adjusting the relative position $y_{average}$ offers greater potential for design optimization.

C. Influence of multi-cavity parallel combination

To broaden the effective sound absorption bandwidth, we maintained the honeycomb geometry from Sec. III A and implemented acoustic impedance coupling via parallel arrangement. Three SHR configurations with distinct parameter sets were investigated. Using the Isight multi-objective optimization (MOP) framework, we defined the optimization parameters as the gradient angle β_∇, micropore diameters (D, d), and spatial positions (w, y_i). The objective functions were set to minimize the resonance frequency while maximizing the half-absorption bandwidth, with weighting factors of 0.6 and 0.4 assigned, respectively, to prioritize low-frequency performance. Manufacturing constraints included micropore diameters ≥ 1.0 mm and fixed cavity depth $H = 15$ mm. Through this approach, the optimal structural parameters summarized in Table II were obtained. A conventional parallel honeycomb structure with identical $D_1 - D_3$ and $w_1 - w_3$ values, but lacking the internal stepped configuration, was designed as a control group [Fig. 8(a)].

Simulation results indicate that the optimized parallel SHR configuration offers pronounced sound absorption advantages in the mid-to-low frequency range (200–1200 Hz). As shown in Fig. 8(d), while the parallel arrangement reduces local performance—decreasing the peak absorption coefficient near resonance by 12% compared to a single unit. This phenomenon can be primarily attributed to the parallel configuration of multiple

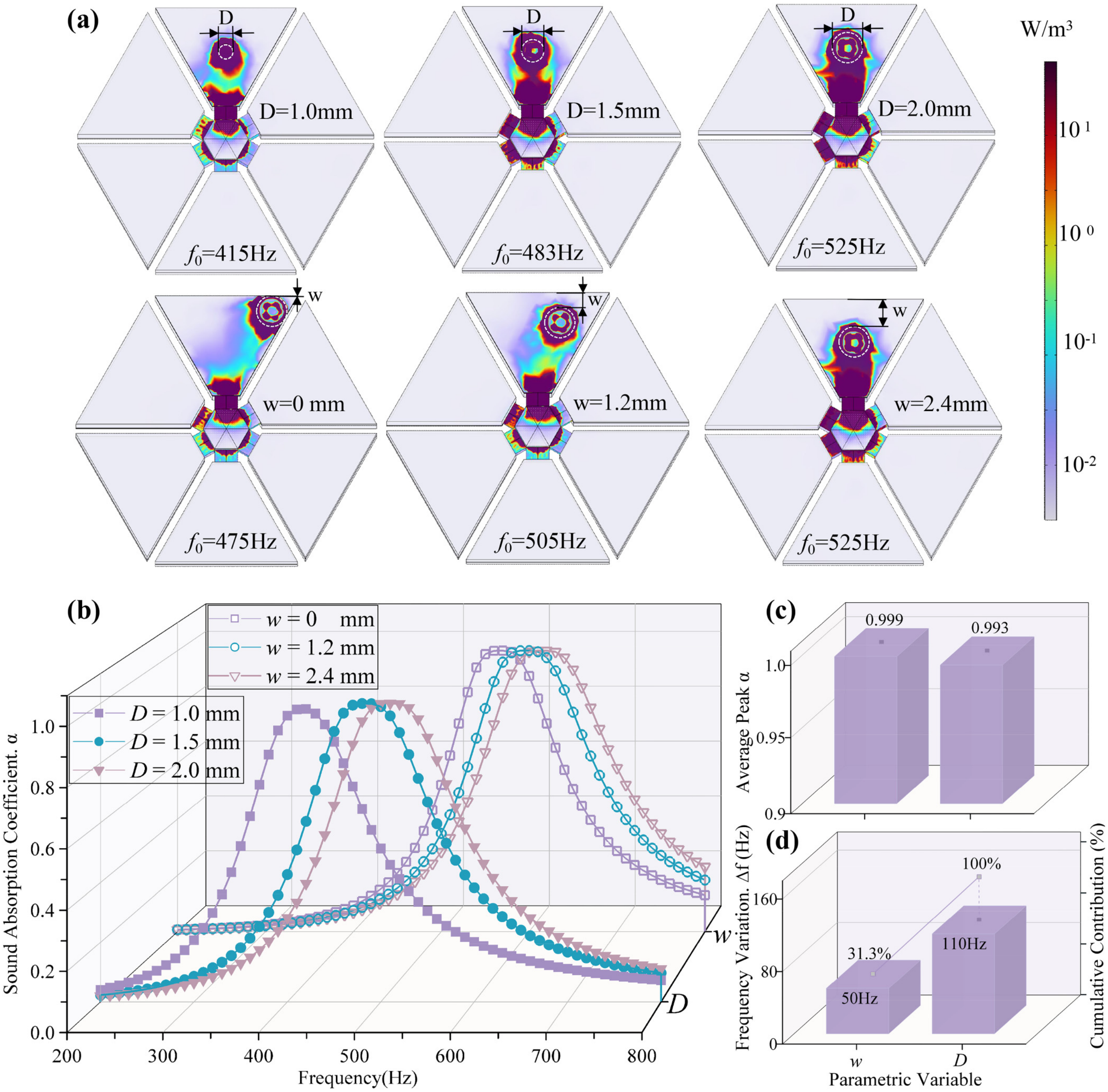

FIG. 6. Acoustic performance of SHR structures with varied top micropore parameters: (a) thermoviscous energy dissipation distribution; (b) sound absorption coefficient; (c) average peak sound absorption coefficient; and (d) Pareto chart.

resonators. Unlike a conventional Helmholtz cavity, which confines energy predominantly to a single frequency, this arrangement distributes acoustic energy across a broader spectral range. Consequently, it compromises localized absorption efficiency and diminishes peak performance at specific resonant frequencies. The optimized parallel SHR configuration substantially broadens the half-absorption bandwidth to 300 Hz (350–650 Hz), representing a 275% increase relative to the single SHR

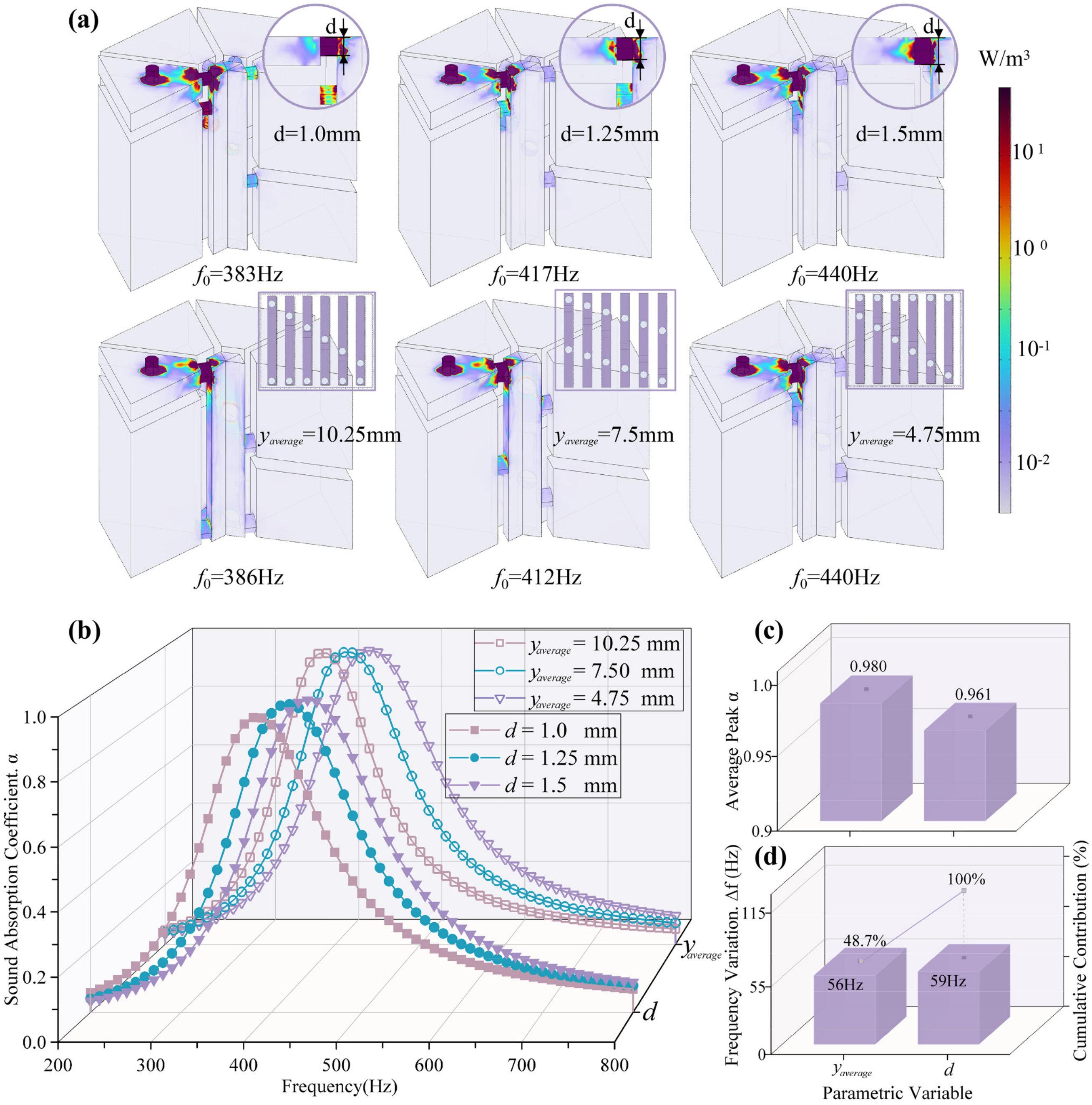

FIG. 7. Acoustic performance of SHR structures with varied middle micropore parameters: (a) thermoviscous energy dissipation distribution; (b) sound absorption coefficient; (c) average peak sound absorption coefficient; and (d) Pareto chart.

structure (80 Hz). Furthermore, although the overall half-absorption bandwidth of the SHR parallel configuration (300 Hz) remains narrower than that of the conventional parallel structure (500 Hz), the SHR design significantly lowers the cutoff frequency for $\alpha > 0.5$ from 580 to 350 Hz—a reduction of 39.6% [Figs. 8(b)–8(c)]. This effectively extends the effective absorption range of the 15 mm-thick metamaterial toward lower frequencies.

TABLE II. Parameters of the SHR parallel combination structure.

Structural groups/parametric	β_∇ (°)	D (mm)	w (mm)	d (mm)	$y_{average}$ (mm)	H (mm)	t (mm)	L (mm)
Structure I	33.7	1.0	0	1.4	10.25	15.0	1.0	10.0
Structure II	31.22	1.5	1.2	1.5	10.25	15.0	1.0	10.0
Structure III	0	2.0	2.4	1.4	10.25	15.0	1.0	10.0

This performance improvement, realized through precise tuning of cavity gradients and micropore geometry, is attributed to the impedance gradient matching characteristics and the synergistic interaction of multiple resonance modes inherent to the SHR architecture. As shown in Table III, compared with representative metamaterial absorbers, the findings demonstrate that the parallel SHR configuration holds practical potential for industrial low-to-mid frequency (350–650 Hz) noise control, while also providing a theoretical basis for developing future broadband sound-absorbing structures with enhanced efficiency.

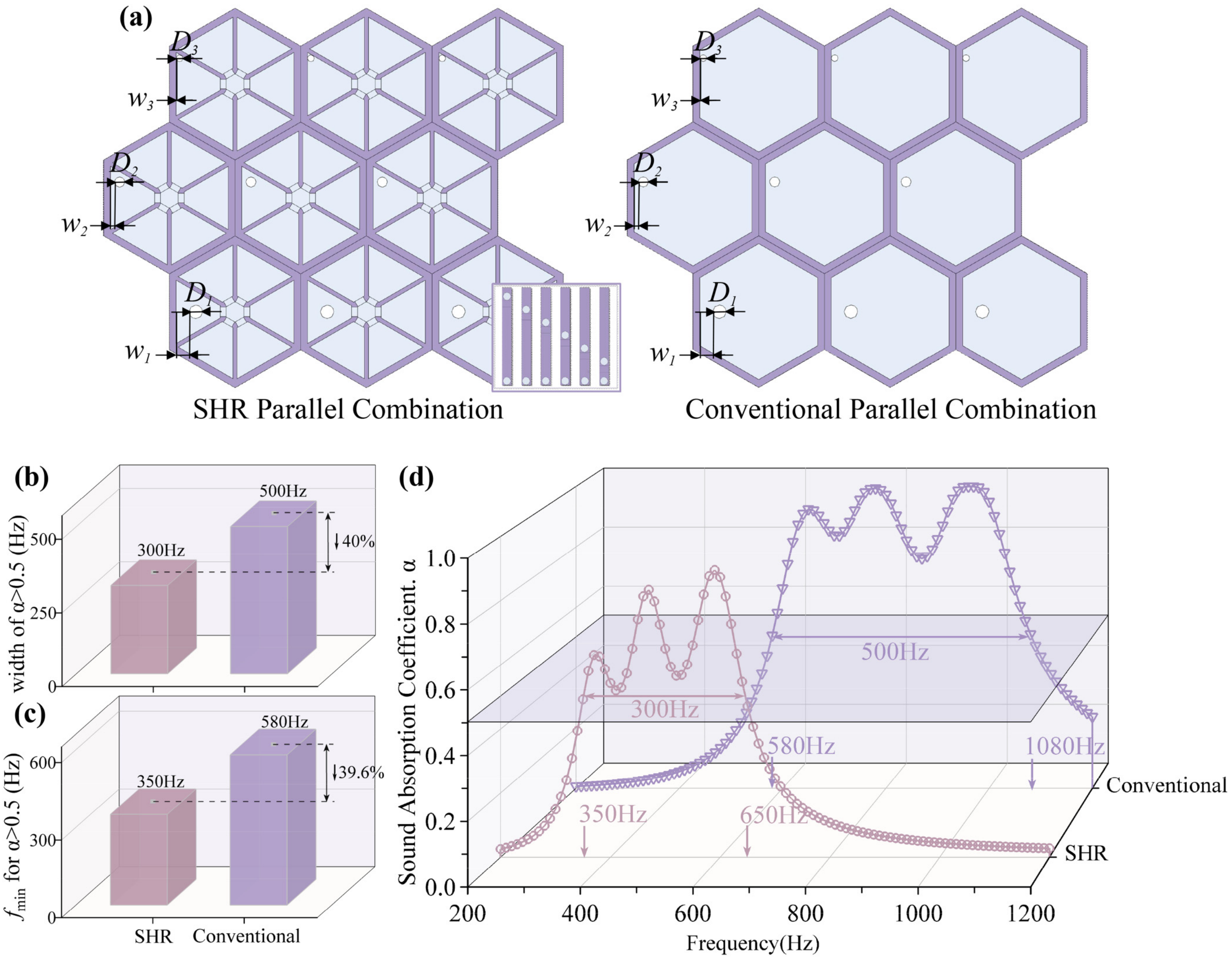

FIG. 8. Performance comparison between SHR parallel combination and conventional parallel combination structures: (a) schematic of parallel combination configuration; (b) half-absorption bandwidth comparison; (c) comparison of lowest frequency (fmin) for $\alpha > 0.5$; and (d) sound absorption coefficient comparison.

TABLE III. Parameters of the SHR parallel combination structure.

Study	Structure type	Thickness (mm)	Peak absorption	Bandwidth (Hz, $\alpha > 0.5$)
Chen *et al.*[26]	Helmholtz resonators with side slits	41.0	0.95	420–970
Kong and Fu[31]	Butterfly double-panel metastructure filled with porous materials	28.0	0.99	380–750
Santos *et al.*[48]	Coupled resonators	24.0	0.98	400–680
Liu *et al.*[49]	A nested and ventilated metasurface based on multi-slit synergetic resonance	39.1	0.90	450–650
This work	Stepped Helmholtz resonators	17.0	0.96	350–530

IV. CONCLUSIONS

This study systematically examines the low-to-mid frequency acoustic performance of honeycomb metamaterials incorporating SHR structures through combined theoretical and numerical approaches. The research elucidates the influence of geometric parameters and structural coupling mechanisms on sound absorption characteristics, with rigorous benchmarking against conventional honeycomb designs. The analysis reveals three principal findings regarding the enhanced acoustic performance of SHR structures in the target frequency range:

- Additively manufactured specimens were experimentally characterized via impedance tube testing. Results confirm that the parametrically designed SHR structure attains a resonance frequency below 440 Hz, representing a 38% reduction compared to conventional honeycomb designs.
- Key dimensional parameters critically govern the acoustic behavior of the SHR structure. The introduced gradient angle enables a 14.3% shift in resonance frequency within a 15 mm cavity depth, offering a novel strategy for low-frequency tuning. Furthermore, reducing micropore diameters effectively lowers the resonance frequency, with the top (D) and middle (d) micropores contributing reductions of 21.4% and 13.0%, respectively. Strategic relocation of micropores closer to inner walls or increasing inter-pore distances also yields significant resonance frequency reduction, providing clear pathways for low-frequency structural optimization.
- Parametric optimization integrating three micropore sizes expanded the half-absorption bandwidth by 275% relative to a single unit, while largely preserving the high peak absorption coefficients of individual elements. The parallel SHR configuration achieves effective absorption ($\alpha > 0.5$) from 350 to 650 Hz, reducing the lower cutoff frequency by 39.6% compared to conventional parallel structures (580 Hz).

AUTHOR DECLARATIONS

Conflict of Interest

The authors have no conflicts to disclose.

Author Contributions

Ziming Song: Conceptualization (equal); Data curation (equal); Formal analysis (equal); Investigation (equal); Methodology (equal); Visualization (equal); Writing – original draft (equal); Writing – review & editing (equal). **Wei Chen:** Methodology (equal); Supervision (equal); Writing – original draft (equal); Writing – review & editing (equal). **Shengzhe Jin:** Conceptualization (equal); Supervision (equal); Validation (equal); Writing – original draft (equal). **Feihu Shan:** Investigation (equal); Supervision (equal). **Kui Liu:** Investigation (equal); Validation (equal). **Hongwei Zhang:** Supervision (equal); Validation (equal). **Sichao Qu:** Data curation (equal); Software (equal); Writing – review & editing (equal).

DATA AVAILABILITY

The data that support the findings of this study are available within the article.

REFERENCES

[1] W. H. Organization *et al.*, *Burden of Disease from Environmental Noise: Quantification of Healthy Life Years Lost in Europe* (World Health Organization, Regional Office for Europe, 2011).
[2] Y. Guan, D. Zhao, and T. S. Low, "Experimental evaluation on acoustic impedance and sound absorption performances of porous foams with additives with Helmholtz number," Aerosp. Sci. Technol. **119**, 107120 (2021).
[3] L. Liu, W. Huang, Y. Zhong, H. Zhao, L. Xie, and X. Yan, "Progress on the research and applications of acoustic metamaterials," Mater. China **40**(1), 57–68 (2021).
[4] B. Gibson, T. Nguyen, S. Sinaie, D. Heath, and T. Ngo, "The low frequency structure-borne sound problem in multi-storey timber buildings and potential of acoustic metamaterials: A review," Build. Sci. **224**, 109531 (2022).
[5] S. Kumar, T. B. Xiang, and H. P. Lee, "Ventilated acoustic metamaterial window panels for simultaneous noise shielding and air circulation," Appl. Acoust. **159**, 107088 (2020).
[6] K. Wang, W. Wang, and X. Yan, "Effect of hole on sound absorption coefficient of micro-perforated panels investigated by melling computing," Concurrency Comput. Pract. Exper. **31**(12), e4725 (2019).
[7] P. Cobo, "Modelling of microperforated panel absorbers with circular and slit hole geometries," in *Acoustics* (MDPI, 2021), Vol. 3, pp. 665–678.
[8] S. Yan, J. Wu, J. Chen, Y. Xiong, Q. Mao, and X. Zhang, "Optimization design and analysis of honeycomb micro-perforated plate broadband sound absorber," Appl. Acoust. **186**, 108487 (2022).
[9] C.-S. Jiang, X.-H. Li, W.-Y. Cheng, Y. Luo, and T. Xing, "Acoustic impedance of microperforated plates with stepwise apertures," Appl. Acoust. **157**, 106998 (2020).
[10] C. Jiang, X. Li, W. Xiao, and B. Zhang, "Acoustic characteristics of microperforated plate with variable cross-sectional holes," J. Acoust. Soc. Am. **150**(3), 1652–1662 (2021).

[11] S. Yan, F. Wu, X. Zhang, M. Hu, Z. Ju, and J. Zhao, "Broaden the sound absorption band by using micro-perforated plate back cavities with different cross-sectional areas," Phys. Scr. **98**(8), 085922 (2023).
[12] X.-L. Gai, T. Xing, X.-H. Li, B. Zhang, Z.-N. Cai, and F. Wang, "Sound absorption properties of microperforated panel with membrane cell and mass blocks composite structure," Appl. Acoust. **137**, 98–107 (2018).
[13] Z. Zhu, L. Ma, C. Li, X. Xie, and J. Hu, "Design and optimization of one special microperforated plate-labyrinth coupled structure (MPPS-LS): From the view of numerical simulation," Int. J. Acoust. Vibr. **29**(2), 193–203 (2024).
[14] H. Liang, G. Zhou, X. Liang, J. Chu, Z. Zhou, W. Wang, and J. Wu, "Study on sound absorption properties of micro perforated plates with acoustic black hole back cavities," Mod. Phys. Lett. B **38**(03), 2350225 (2024).
[15] X. Li, L. Ma, J. Hu, and Z. Zhu, "Design a special micro-perforated plate coupled with the labyrinth metamaterial with improved sound absorption properties at medium and low frequencies," Mod. Phys. Lett. B **38**(07), 2450021 (2024).
[16] C. Jiang, "Investigation on acoustic performance of distributed periodic micro perforated panel," Noise Control Eng. J. **72**(2), 131–149 (2024).
[17] H. Yan, S. Xie, Z. Li, Z. Feng, K. Jing, and F. Zhang, "Enhanced sound absorption performance of stepped-type multi-cavity acoustic absorbers using a hybrid particle swarm algorithm," J. Vibr. Control **30**(13–14), 3233–3246 (2024).
[18] C. Liu, X. Liu, Z. Xie, J. H. Wu, and F. Ma, "A tunable high-order microperforated panel metamaterial with low-frequency broadband acoustic absorption," Appl. Phys. Express **17**(8), 084001 (2024).
[19] L. Shen, Y. Zhu, F. Mao, S. Gao, Z. Su, Z. Luo, H. Zhang, and B. Assouar, "Broadband low-frequency acoustic metamuffler," Phys. Rev. Appl. **16**(6), 064057 (2021).
[20] C. Song, S. Huang, Z. Zhou, J. Zhang, B. Jia, C. Zhou, Y. Li, and Y. Pan, "Perfect acoustic absorption of Helmholtz resonators via tapered necks," Appl. Phys. Express **15**(8), 084006 (2022).
[21] J. Zhu, Y. Qu, H. Gao, and G. Meng, "Nonlinear sound absorption of Helmholtz resonators with serrated necks under high-amplitude sound wave excitation," J. Sound Vibr. **537**, 117197 (2022).
[22] S. Yan, F. Wu, X. Zhang, D. Zhang, and Z. Wu, "Rectangular extended neck Helmholtz resonant acoustic structure for low frequency broadband sound absorption," Phys. Scr. **99**(7), 075004 (2024).
[23] S. Bi, E. Wang, X. Shen, F. Yang, X. Zhang, X. Yang, Q. Yin, C. Shen, M. Xu, and J. Wan, "Enhancement of sound absorption performance of Helmholtz resonators by space division and chamber grouping," Appl. Acoust. **207**, 109352 (2023).
[24] X. Yang, X. Shen, F. Yang, Z. Yin, F. Yang, Q. Yang, C. Shen, M. Xu, and J. Wan, "Acoustic metamaterials of modular nested Helmholtz resonators with multiple tunable absorption peaks," Appl. Acoust. **213**, 109647 (2023).
[25] S. Nakanishi, "Broadband sound absorption by acoustic metasurface of planar array of small Helmholtz resonators," Acoust. Sci. Technol. **45**(4), e24-11 (2024).
[26] X. Chen, F. Sun, J. Zhang, G. Chen, L. Xu, L. Fan, L. Cheng, X. Xu, Y. Chen, J. Zhou *et al.*, "A compact acoustic metamaterial based on Helmholtz resonators with side slits for low-frequency sound absorption," Appl. Phys. Lett. **125**(1), 013502 (2024).
[27] C. Song, X. Ma, J. Zhao, J. Zhang, F. Yang, Y. Pan, and X. Zhang, "Broadband sound absorption and energy harvesting by a graded array of Helmholtz resonators," IEEE Trans. Dielectr. Electr. Insul. **29**(3), 777–783 (2022).
[28] J. Zhang, T. Chen, F. Xin, J. Zhu, and W. Ding, "New-parallel connection of the Helmholtz resonator with embedded apertures for low-frequency broadband sound absorption," Jpn. J. Appl. Phys. **61**(7), 077001 (2022).
[29] S. Bi, F. Yang, S. Tang, X. Shen, X. Zhang, J. Zhu, X. Yang, W. Peng, and F. Yuan, "Effects of aperture shape on absorption property of acoustic metamaterial of parallel-connection Helmholtz resonator," Materials **16**(4), 1597 (2023).
[30] W. Zhang and F. Xin, "Broadband low-frequency sound absorption via Helmholtz resonators with porous material lining," J. Sound Vibr. **578**, 118330 (2024).
[31] W. Kong and T. Fu, "A novel butterfly double-panel metastructure filled with porous materials for broadband low-frequency sound absorption," J. Build. Eng. **97**, 110935 (2024).
[32] X.-L. Gai, X.-W. Guan, Z.-N. Cai, X.-H. Li, W.-C. Hu, T. Xing, and F. Wang, "Acoustic properties of honeycomb like sandwich acoustic metamaterials," Appl. Acoust. **199**, 109016 (2022).
[33] Z. Liu, C. Dong, L. Tong, C. Rudd, X. Yi, and X. Liu, "Sound absorption performance of ultralight honeycomb sandwich panels filled with 'network' fibers—*Juncus effusus*," Polymers **16**(13), 1953 (2024).
[34] L. Zhang, W. Zhang, and F. Xin, "Broadband low-frequency sound absorption of honeycomb sandwich panels with rough embedded necks," Mech. Syst. Signal Process. **196**, 110311 (2023).
[35] S. Qiu, H. Ding, T. Lu, S. Liu, P. Qian, N. Wang *et al.*, "Honeycomb acoustic liner based on embedded apertures and multi-depth cavities," Chin. Sci. Bull. **68**, 3482–3490 (2023).
[36] H. Yan, S. Xie, F. Zhang, K. Jing, and L. He, "Semi-self-similar fractal cellular structures with broadband sound absorption," Appl. Acoust. **217**, 109864 (2024).
[37] R. Kang, C. Shen, and T. J. Lu, "A three-dimensional theoretical model of free vibration for multifunctional sandwich plates with honeycomb-corrugated hybrid cores," Compos. Struct. **298**, 115990 (2022).
[38] A. Haris and H. P. Lee, "Sound transmission loss and compression properties of sandwich panels with milli-perforated honeycomb core," Fibers Polym. **23**(11), 3138–3145 (2022).
[39] D.-Y. Maa, "Potential of microperforated panel absorber," J. Acoust. Soc. Am. **104**(5), 2861–2866 (1998).
[40] H. Yan, S. Xie, F. Zhang, K. Jing, and L. He, "Sound absorption performance of honeycomb metamaterials inspired by Mortise-and-Tenon structures," Appl. Acoust. **228**, 110292 (2025).
[41] J. Huang, J. Wang, T. Ma, H. Wei, S. Zhang, G. Wang, L. Wang, Q. Wang, W. Zhou, and Z. Zhang, "Composite structure with porous material and parallel resonators for broadband sound absorption at low-to-mid frequencies," Appl. Acoust. **225**, 110193 (2024).
[42] U. Ingard, "On the theory and design of acoustic resonators," J. Acoust. Soc. Am. **25**(6), 1037–1061 (1953).
[43] D. Maa, "Theory and design of microperforated panel sound-absorbing constructions," Sci. China Ser. A. **18**(1), 55–71 (1975).
[44] S. Mukae, T. Okuzono, K. Tamaru, and K. Sakagami, "Modeling microperforated panels and permeable membranes for a room acoustic solver with plane-wave enriched FEM," Appl. Acoust. **185**, 108383 (2022).
[45] H. Zhao, Q. Zheng, Y. Wang, J. Cao, C. Wang, and J. Wen, "Acoustic absorption of a metamaterial panel: Mechanism, boundary effect and experimental demonstration," Appl. Acoust. **184**, 108369 (2021).
[46] K. Uenishi, T. Okuzono, and K. Sakagami, "Finite element analysis of absorption characteristics of permeable membrane absorbers array," Acoust. Sci. Technol. **38**(6), 322–325 (2017).
[47] T. Okuzono, N. Shimizu, and K. Sakagami, "Predicting absorption characteristics of single-leaf permeable membrane absorbers using finite element method in a time domain," Appl. Acoust. **151**, 172–182 (2019).
[48] L. A. Santos, G. do Nascimento Almeida, E. F. Vergara, L. R. Barbosa, and L. C. B. Farias, "Meta-structure based on coupled resonators for low-frequency broadband sound absorption," Acta Sci. Technol. **46**(1), e64257 (2023).
[49] H. Liu, J. H. Wu, and F. Ma, "High-efficiency sound absorption by a nested and ventilated metasurface based on multi-slit synergetic resonance," J. Phys. D: Appl. Phys. **54**(20), 205304 (2021).